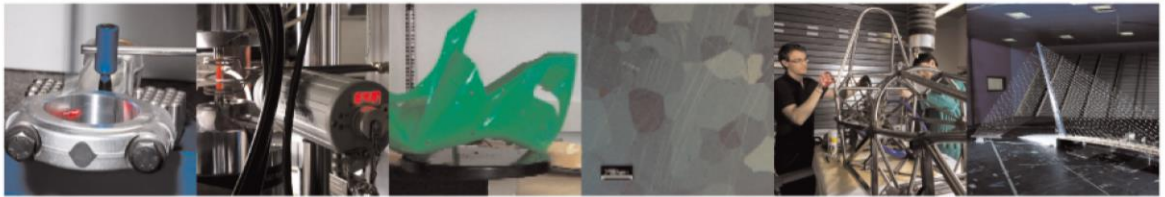POLITECNICO
MILANO 1863

DIPARTIMENTO DI MECCANICA

mecc

A comprehensive study of A357 alloy printability via laser metal deposition

Furlan, V.; Kurtay, T.; Grande, A. M.; Previtali, B.

A comprehensive study of A357 alloy printability via Laser Metal Deposition

Valentina Furlan[1*], valentina.furlan@unipv.it
Tugay Kurtay[2], tugaykurtay@gmail.com
Antonio Mattia Grande[3], antoniomattia.grande@polimi.it
Barbara Previtali[2], barbara.previtali@polimi.it

[1] Department of Electrical Computer and Biomedical Engineering, Università di Pavia, Via Ferrata 5, 27100 Pavia, Italy
[2] Department of Mechanical Engineering, Politecnico di Milano, Via La Masa 1, 20156 Milan, Italy
[3] Department of Aerospace Science and Technology, Politecnico di Milano, Via La Masa 34, 20156 Milan, Italy
*Corresponding author

A comprehensive study of A357 alloy printability via Laser Metal Deposition

Valentina Furlan[1*], valentina.furlan@polimi.it

Tugay Kurtay[2], tugaykurtay@gmail.com

Antonio Mattia Grande[3], antoniomattia.grande@polimi.it

Barbara Previtali[2], barbara.previtali@polimi.it

[1]Department of Electrical Computer and Biomedical Engineering, Università di Pavia, Via Ferrata 5, 27100 Pavia, Italy
[2]Department of Mechanical Engineering, Politecnico di Milano, Via La Masa 1, 20156 Milan, Italy
[3]Department of Aerospace Science and Technology, Politecnico di Milano, Via La Masa 34, 20156 Milan, Italy
*Corresponding author

Abstract

Laser metal deposition (LMD) is one of the most important techniques in additive manufacturing (AM) thanks to the high flexibility of the process, which makes the production of free-form shapes possible. However, working with some materials presents some challenges. This is the case with aluminum alloys due to their reflectivity and their very high thermal conductivity. On the other hand, aluminum and its alloys are quite important in several industrial fields, including aerospace, among others, due to their mechanical properties with low density. In this work, LMD is applied on an A357 aluminum alloy. The techniques are investigated moving from a single-track approach up to multi-pass and multi-layer strategies. Densities, microstructures and mechanical performance are investigated as a function of process parameters. Porosities are reduced, resulting in overall densities of over 97% and microhardness values in the range of 80-100 HV. Differences in mechanical performance are analysed considering different building directions, showing a dependency on loading direction and the distance from the substrate. Tensile tests reveal a promising performance for further investigation with the LMD technique. The obtained evidence is interesting for future trends where large and light components are required while maintaining the mechanical performance of traditional manufacturing methods. Moreover, a comprehensive study is done for the first time on A357 alloy that is deeply used in the aerospace and automotive fields. The investigation and definition of best process parameters open the possibility of exploiting LMD technology in the production of wide components or for adding features to already existing components overcoming some limits of other AM technologies.

Keywords: Laser Metal Deposition, Aluminum, Additive Manufacturing, Mechanical Properties

Introduction

Additive manufacturing (AM) is a fast-growing trend in the industry. Laser metal deposition (LMD) is a laser-based additive manufacturing method that can fabricate large, free-form and possibly multi-material metallic components. This ability is particularly interesting in aerospace an automotive fields with a direct comparison with traditional manufacturing methods for composite materials [1], [2]. Contrary to selective laser melting (SLM), which uses a powder bed approach, in LMD the powder is delivered simultaneously through the nozzle, a focused laser beam melts the powder and a layer-by-layer approach permits the building of 3D parts. LMD is a flexible approach that has a high potential to produce components for the aerospace, medical and automotive industries. As for the other AM processes, in LMD the quality of printed parts, taking into account anisotropy and heterogeneity, is a crucial aspect. Cyclic thermal history affects LMD parts, resulting in an intrinsic anisotropy of the printed parts [3], [4]. Moreover, porosity is another common concern that affects the mechanical properties of metallic printed parts. Depending on the application field, LMD can work with several metallic powders, such as titanium alloys, steels, nickel-based super-alloys, cobalt-based alloys, copper alloys and aluminum alloys [5], [6], [7], [8]. However, some powder materials present critical aspects, as is the case for aluminum alloys; the LMD of aluminum alloys is still challenging. The main issues are related to the intrinsic material properties and the characteristics of the LMD process. The interaction between aluminum alloys and laser is complex. The aluminum surfaces are highly reflective of laser radiation and the thermal conductivity of aluminum is very high [9], [10], [11]. The reflectivity of the material requires high laser power density to achieve the melting of powders and substrate; however, the increase in energetic content is detrimental to the density of the printed part. High energy can promote the evaporation of alloying elements like magnesium or zinc, which are common in commercial powders and result in porosities [11]. On the other hand, the high laser energy is also a major cause of issues such as cracks [11].

Moreover, aluminum powders processed by LMD require a protective atmosphere. Safety and quality aspects are crucial. The size of aluminum powders for LMD can promote material reactivity; the powders can explode or burn. Furthermore, printed parts always require a high standard of quality; this means low absorption of oxygen, which can be detrimental to the mechanical performance [12]. In addition, the aluminum oxides are characterised by a higher melting point that can still cause porosities and inclusions. Lastly, aluminum powders are characterised by a low density and are commonly affected by issues of flowability due to their high moisture absorption. This aspect is directly related to porosities caused by hydrogen formation [11], [13].

Despite all of these critical aspects, aluminum alloys are still promising. They have good properties, like high corrosion resistance and high strength to weight ratio; these make aluminum alloys favourable in the automotive and aerospace industries [14], [15]. Considering the different aluminum alloys, A357 is one of the most widely used in the aerospace and automotive industries; it is used in cast components, such as brackets, carters and stands [16]. A357 is relatively easier to process compared with other aluminum alloys in laser applications due to the lower difference between solidus and liquidus temperatures [17]. The addition of silicon (Si) minimises shrinkage and increases castability, while magnesium (Mg) promotes the formation of Mg_2Si precipitates that increase the strength of the alloy. However, the A357 alloy has some challenges for production with LMD.

In literature, there are few studies on LMD and aluminum alloys due to the tendency of porosity formation [18]. The main articles are on Al-Si alloys and process parameters with metallurgical and microstructural analyses [19], [20]. Metallographic investigation revealed that the microstructural morphology strongly depends on the location of the deposit and on process parameters. Different temperature gradients and solidification velocities promote these differences, but high density values are obtainable [19], [21], [22]. Some articles investigate the LMD process on AlSiMg alloys that are more similar in chemical content to A357. The AlSi10Mg is the most investigated alloy in terms of parameters, metallurgy and microstructures, and mechanical performance [20]. Javidani *et al.* examined AlSi10Mg alloy microstructures in various locations of the whole deposit [23]. They conducted microhardness tests to study the hardness gradient in the specimen along the deposition

direction, concluding that the hardness value decreases as the deposition height increases. Chen *et al*. investigated the effect of the scanning speed on the microstructure and tensile properties of the AlSi10Mg alloy parts deposited with optimised parameters [24]. Different fracture surfaces were observed, revealing defects such as unmelted powders and pores. Moreover, the tensile properties gradually strengthened by reducing the scanning speed, exceeding the tensile properties achievable through casting (i.e. UTS=162 MPa and UTS=145 MPa for LMD and casting, respectively) [24], [25]. Lv *et al*. studied the effects of heat treatments on the mechanical properties of LMD-built AlSi10Mg dog bone samples. They examined tensile properties and obtained increased strength values when the samples were heat treated [26]. It is interesting to observe that although AlSi10Mg has a similar chemical content to A357 alloy, the Si content is 3% higher, which affects precipitation and microstructural evolution. Hence, these studies cannot be taken as a precise reference for A357 alloy. Besides, apart from porosity formation, other possible problems such as alloying element evaporation and working environment conditions that might cause low mechanical properties are not discussed in detail in the literature for the LMD of Al alloys. Therefore, the main works on the AM of A357 alloy are focused on the selective laser melting (SLM) method. These works study the effect of process parameters on density, microstructure and mechanical properties [16], [17]. Yang et al. investigated the influence of heat treatments on the microstructure and mechanical properties of A357 alloy [15]. Nevertheless, A357 was also investigated with gas metal arc welding (GMAW). Cao et al. investigated the microstructure and the crack formation of the weld through gas metal arc welding (GMAW) [27]. Although there are studies dealing with A357 alloy fabricated by two different AM processes (i.e. SLM and GMAW), the mechanical properties and chemical structures are different from those obtained by the LMD process. In SLM, the cooling rate is higher than in the LMD process. While the cooling rate reaches a magnitude of 10^5-10^6 K/s in the SLM process [15], [28], [29], this value is about 10^3-10^4 K/s in the LMD process, which is 100 times slower than SLM [19], [30]. On the contrary, in GMAW, the cooling rate is lower than in LMD [31], [32].

In this paper, a complete investigation of the LMD on the A357 alloy is presented. The main challenge is the material, which is characterised by 94.1% reflectivity at room temperature and defect formation [33]. Moreover, risks of oxidation and hydrogen entrapment when temperatures are high (i.e. LMD) require a dedicated inert working environment. Experiments investigate the effect of process parameters on the quality of the deposits. The process design, execution and analyses are based on an empirical approach and statistical methods. Firstly, porosities and densities and microstructures and microhardness are investigated. Then, tensile tests on best parameters are provided to investigate the mechanical performances of LMD parts. Through this experimental and empirical analysis, the nature of the problems associated with the LMD of A357 is addressed, and the current limitations and constraints of the process are highlighted to provide a preliminary guideline for the manufacturing of large components with LMD and A357 alloy.

Materials and methods
1.1 Materials
In this study, gas-atomised A357 aluminum alloy supplied by LPW (Carpenter Technology Corporation, Philadelphia, USA) is used. Table 1 shows the chemical composition of the aluminum alloy as declared by the producer. Malvern Panalytical Morphology 4 (Malvern Instruments Limited and Panalytical B.V., Malvern, UK) determines the powder characteristics. The power granulometry is 45-90 µm. The average powder diameter is 70.02 µm with a standard deviation of 28.34 µm. A scanning electron microscope (SEM, EVO-50 Carl Zeiss by Carl Zeiss AG, Oberkochen, Germany) shows the powder morphology (Fig. 1a), revealing that the powder is not perfectly spherical and has satellites. The aspect ratio in Fig. 1b confirms the elongated shapes of the powder. The substrates used are series 5000 with a thickness of 10 mm.

Elements	Mg	Si	Ti	Cu	Fe	C	Zn	Other	Al
Nominal wt%	0.65	7.1	0.09	0.01	0.07	0.06	0.02	0.01	Bal.

Table 1: Chemical composition of A357 alloy (wt%)
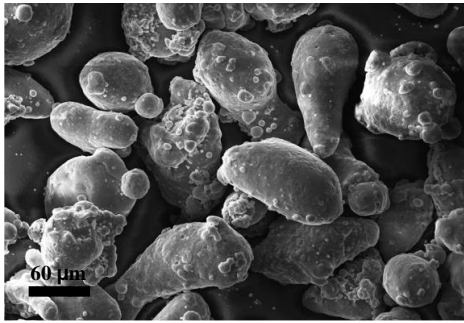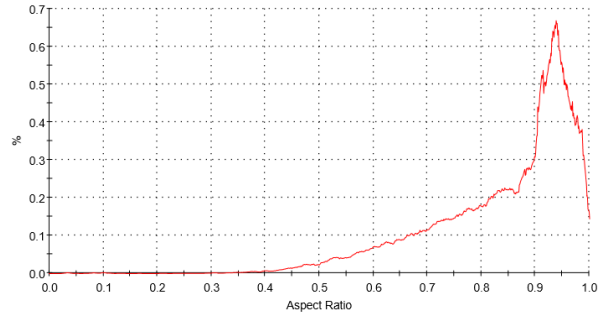
(a) *(b)*

Figure 1: A357 alloy, powder morphology with 1000x magnification (a) and aspect ratio measurement (b).

1.2 LMD System

The employed LMD system consists of an anthropomorphic robot with 6 axes (i.e. ABB IRB 4600 - 45/2.05 by ABB Robotics, Zurich, Switzerland) and a 2-axis rotary and tilting table (i.e. ABB IRBP A-250 by ABB Robotics, Zurich, Switzerland). The MWO-I-Powder deposition head (by KUKA Laser, Augsburg, Germany) is mounted on the anthropomorphic robot. The head is equipped with a 129 mm focal length lens to collimate the laser beam and a 200 mm focal length lens to focus it on the working area. The collimation unit is variable in position, resulting in different spot dimensions at the target plane for a fixed standoff distance. The deposition head includes a three-jet nozzle (Fraunhofer ILT 3- JET-SO16-S) for powder delivery. A powder feeder (GTV TWIN PF 2/2-MF) controls the powder flow. Argon is used as a carrier gas to deliver the powder from the feeder to the nozzle. During the process, argon is also used as shielding gas. The employed fibre laser source is the IPG YLS 3000 (YLP-1/100/50/50 IPG Photonics Corporation, Oxford, Massachusetts, USA), characterised by 3 kW maximum power and 1070 nm emission wavelength. A 400 μm processing fibre delivers the laser radiation to the deposition head. The LMD system is also equipped with a flexible chamber to control the LMD environment, avoiding contamination with ambient gases (i.e. oxygen and hydrogen) as well as explosion/fire hazards. The chamber is fixed to the deposition head by a coupler made in-house. The chamber is a flexible enclosure from Huntingdon Fusion Techniques that can withstand up to 250° C. The argon fills the chamber with four diffusers. The diffusers are evenly spaced on a circular base plate. The circular base plate works as a structural base where the substrate can be placed in the central part. The plate is helpful and protects the plastic chamber from the sparks created during the process. The four argon flows merge in a laminar way in the centre of the chamber, forming a preferential path for the purge gas to exit through the holes on the support disk. Two oxygen sensors are used to detect the oxygen content. The first sensor (Protégé ZM by Scott Safety) operates in the order of magnitude of 1 unit of volumetric percentage, and its minimum resolution is 0.1 percentage point. It is used to check that the percentage of oxygen does not exceed a threshold value set to ensure safe processing without hazards. The second sensor (Putgeye 300 nano by Huntingdon Fusion Techniques) operates in the magnitude of 100 parts per million of volumetric percentage, with a minimum resolution of 10 parts per million. It is more sensitive and it is used to check the oxygen content near the melt pool. It is used to avoid the thermal oxidation of the printed part and measures by means of a pump. The pump samples the chamber gas and sends it through a tube to a remote monitor, which permits the continuous reading of the ppm during deposition. Fig. 2

shows the anthropomorphic robot with the deposition head and the flexible chamber. Table 2 reports the main characteristics of the LMD setup and the main fixed parameters for the experiments.

Figure 2 LMD system equipped with the flexible chamber

Main characteristics of the LMD Setup	
Maximum laser power, P_{max} [kW]	3
Laser wavelength, λ [nm]	1070
Beam parameter product, BPP [mm·mrad]	16.1
Processing fibre diameter, d_{fp} [μm]	400
Collimation lens length, f_c [mm]	129
Focusing lens length, f_f [mm]	200
Main fixed parameters in the experimental campaigns	
Reference standoff distance, SOD [mm]	12
Waist diameter, d_0 [mm]	0.77
Spot diameter at the target plane, d_w [mm]	1.2
Chamber gas flow rate, $g_{chamber}$ [l/min]	60
Reference of safety oxygen percentage, ox_s [%]	<4
Reference of quality oxygen content, ox_q [ppm]	100

Table 2 Characteristics of LMD system and main fixed parameters in the experimental campaign

1.3 Experimental campaign and characterisations

Considering the complexity of the interaction between aluminum powders and a laser beam, the LMD of A357 needs structured experimental campaigns to determine feasibility windows and best parameters. The study of LMD is done in steps at different levels of complexity. The first preliminary step is the single-track fabrication as a function of main parameters: power, speed, powder flow rate and shielding gas flow rate. Single-track studies are a mandatory step for the LMD process. The strategies in 3D printing are based on tracks and layers that overlap in different directions (i.e. x, y and z). A correct overlap requires track investigation. Their shape, as much as their dimension and density, affect the fabrication when tracks are overlapped and layers built-up. The feasibility window of single tracks is followed by an experimental campaign on 3D shapes. Multi-pass and multi-layer components present different complexities. The thermal load changes and defects can be generated

like porosities due to either a lack of fusion or overheating, as well as by gases [20]. Moreover, anisotropy and different mechanical properties occur as a function of build direction. Therefore, an experimental campaign is designed and executed in which simple cubes are printed and qualified in order to define the best set of process parameters. Indeed, cubes are considered representative of multi-pass and multi-layer approaches. They are useful for the further analysis of the mechanical properties of 3D parts, referring to density and microhardness evaluations. Finally, parallelepipeds are printed both vertically and horizontally to extract tensile specimens and characterise their static mechanical performance.

The next sub-paragraphs describe the three phases of the LMD investigation: i) single-track coupons ii) cube coupons iii) tensile test coupons.

1.3.1 Single-track experiments

A preliminary experimental campaign on single-track fabrication is conducted. Laser power (P), speed (v), powder flow rate (g_{powder}) and shielding gas flow rate ($g_{shielding}$) are varied parameters. The shielding gas is important to protect the melt pool from oxidation; it must therefore not cause porosities on tracks. The carrier gas flow rate ($g_{carrier}$) is fixed at 7.5 l/min. The relative densities of single tracks are evaluated. The aim of this preliminary study is to have a process map showing relative density and track morphologies. Table 3 shows fixed and varied parameters. The experimental campaign is a 2^4 factorial design without replication , resulting in 16 conditions.

Fixed parameter	
Carrier gas flow rate, $g_{carrier}$ [l/min]	7.5
Varied parameter	
Power, P [W]	700-900
Speed, v [mm/s]	15-30
Shielding gas flow rate, $g_{shielding}$ [l/min]	11-25
Powder feed rate, g_{powder} [g/min]	1.8-4.2

Table 3 Varied and fixed parameters of single tracks experimental campaign.

The relative density of printed tracks is measured. Three cross-sections are produced in different positions for each experimental condition. The cross-sections are polished to measure the relative density by an optical method. An optical microscope is utilised, namely the Mitutoyo Quick Vision Pro (Mitutoyo Corporation, Tokyo, Japan), to acquire the cross-sectional views of tracks. The acquisitions are performed with an objective lens of 2.5X. ImageJ software is used for image analysis. The cross-sectional views are binarised by setting the threshold. After the binarisation, the pores are visualised with a white colour and the dense material with black. Consequently, the pores can be identified. As a result, the relative density of tracks can be calculated. Although this approach does not provide information for the whole volume, the information from the three sections describes the trend. On the other hand, this method permits the evaluation of pores in terms of shape, dimension and distribution, and it is the sole method for determining the relative density values of single tracks because of their small dimensions [34].

1.3.2 Multi-pass and multi-layer experiments

Multi-pass and multi-layer experiments are performed to determine the feasibility window for printing 3D objects. Simple 3D geometries (i.e. cubes) are printed. The values for the laser power, speed, powder feed rate and shielding gas flow rate are established according to the results of the preliminary experimental campaign on single tracks. The cubes have a dimension of 10x10x10 mm^3. A bidirectional scanning strategy and alternated layers are used. The overlap between two consecutive tracks (ov_t) and the overlap between two consecutive layers are fixed and they can be calculated as:

$$ov_t = \frac{w-t}{w} \cdot 100 \ \text{ and } \ ov_l = \frac{h-l}{h} \cdot 100$$

where w is the track width, t is the distance between two consecutive passes, h is the track height and l is the distance between two consecutive layers (referring to Fig. 3).
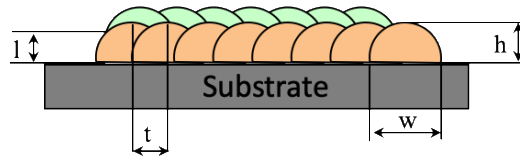

Figure 3 Tracks and layers overlap definition

The value for the ov_t and the ov_l were determined by a previous experimental campaign.

The varied parameter is the carrier gas flow rate. Four levels of carrier gas flow rate are inspected, and three replications are completed for each level. In multi-pass and multi-layer, the carrier gas can affect printability, especially in the case of light and highly reactive elements like aluminum. The carrier gas can affect the dynamic of powders, resulting in possible porosity issues[35]. Three replicas for each condition are provided. Fig. 4 shows the bidirectional strategy and the cubic sample deposit with the layer's alternation.
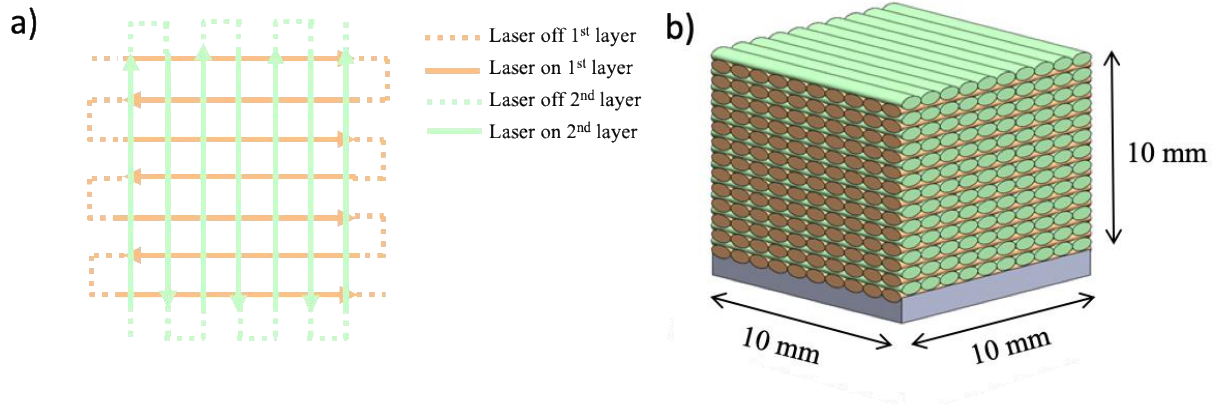

Figure 4 Cubic sample deposit: a) Detail of the adopted scanning strategy with laser on and off phases, b) Alternated build-up.

Table 4 shows fixed and varied parameters.

Fixed parameter	
Power, P [W]	900
Speed, v [mm/s]	30
Powder feed rate, g_{powder} [g/min]	4.2
Shielding gas flow rate, $g_{shielding}$ [l/min]	25
Tracks overlap, ov_t [%]	45
Layer overlap, ov_l [%]	80
Varied parameter	
Carrier gas flow rate, $g_{carrier}$ (l/min)	4.5– 5.5 – 6.5 – 7.5

Table 4 Varied and fixed parameters of multi-pass and multi-layer experiment.

The density of the cubes is measured using the Archimedes method. Obtained values are converted to relative density by considering 2.68 g/cm^3 as the nominal density value of A357 alloy [17], [36], [37]. The three replicas of best condition are cut, resulting in a cross-section portion. The samples are polished up to mirror surfaces and they are etched with Keller's etchant (95 mL H_2O, 2.5 mL HNO_3, 1.5 mL HCl, 1.0 mL HF) to reveal microstructure and grain boundaries. The SEM image of cross-sectioned cubes shows the obtained microstructure (EVO-50 from Carl Zeiss, Oberkochen, Germany). The chemical composition of cross-sectioned cubes is assessed using energy dispersive X-ray spectroscopy (EDS, Inca Energy 200 from Oxfod Instruments, Abingdon, UK). Microhardness

is measured by the Vickers microhardness test, applying a 300 g load for 15 seconds on three different positions (i.e. bottom [0-3 mm], middle [3-6 mm] and top [7-10 mm] on the cross-sections). Hardness tests are performed according to ISO 6507-1:2005. The three different positions permit the evaluation of different mechanical behaviour as a function of the position and the cooling rate. For each section of the cubes, 10 measurements are carried out.

In this way, the influence of the position can be investigated. In fact, the bottom is closed to the substrate, resulting in a different cooling rate in comparison to the middle and the top. On the other hand, the top presents a different dissipation and differences are expected.

1.3.3. Evaluation of static mechanical performance of printed specimens

Tensile tests are performed to determine static mechanical properties of the LMD-fabricated A357 alloy deposited with optimised parameters (Table 5). Two parallelepipeds (i.e. 17x17x117 mm^3) are printed vertically and horizontally, respectively (see Fig. 5), adopting the same bidirectional scanning strategy with alternated layers. The two directions permit the evaluation of different specimens' behaviours as a function of employed strategy. The parallelepipeds are thermally treated after their fabrication to reduce the internal stress. The stress-relieving procedure is characterised by 2 hours at 300°C in air. Fig. 5 shows tensile test coupon dimensions according to the standard ASTM E8. The tensile dog bone-shaped specimens are extracted by a fine wire electro discharge machining (EDM) process from prismatic precursors as shown in Fig. 6. The advantage of using EDM is that it helps in removing the confounding effect due to the external surface roughness. Four dog bone-shaped specimens are extracted from the vertical parallelepiped and four dog bone-shaped specimens are extracted for the horizontal one. The eight dog bones are measures in terms of density with Archimedes' methods. Each dog bone-shaped specimen is cut along vertical and horizontal direction to identify variations in the microstructure depending on the deposition direction. Further analysis is performed using an optical microscope and the SEM. The optical microscope is utilised, namely the Mitutoyo Quick Vision Pro (Mitutoyo Corporation, Tokyo, Japan), to acquire the cross-sectional of a portion of dog bone-shaped specimen. The acquisitions are performed with an objective lens of 2.5X. ImageJ software is used for image analysis. The cross-sectional views are binarised by setting the threshold. After the binarisation, the pores are visualised with a white colour and the dense material with black. Consequently, the pores can be identified. The image of each cross-section is analysed to collect information on pores distribution and dimensions. Moreover, the SEM image of cross-sections shows the obtained microstructure (EVO-50 from Carl Zeiss, Oberkochen, Germany). The SEM is also used to analyse the surface fracture of tensile specimens.

Power, P [W]	900
Speed, v [mm/s]	30
Powder feed rate, g_{powder} [g/min]	4.2
Shielding gas flow rate, $g_{shielding}$ [l/min]	25
Carrier gas flow rate, $g_{carrier}$ (l/min)	5.5
Tracks overlap, ov_t [%]	45
Layer overlap, ov_l [%]	80

Table 5 Set of best process parameters for laser metal deposition of A357 alloy.
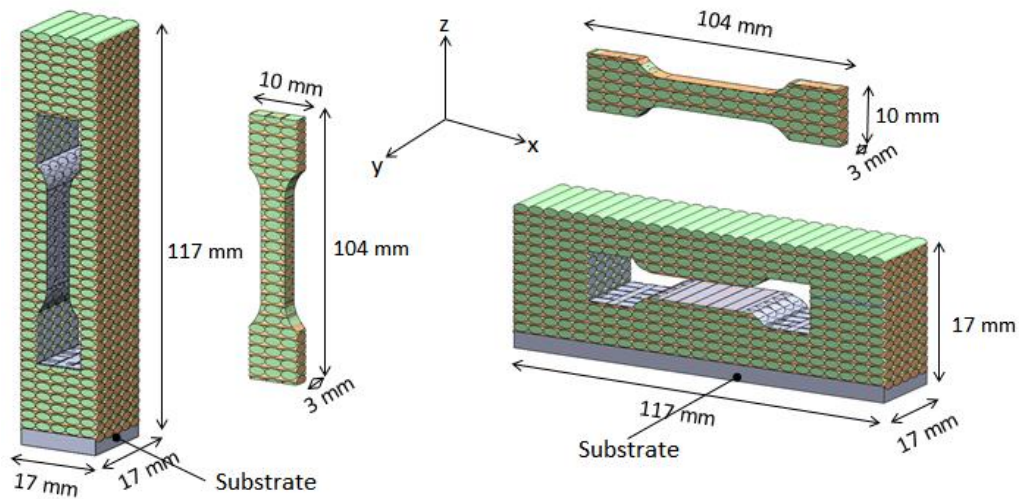
Figure 5: Deposit of vertical and horizontal prismatic sample as precursor of vertical and horizontal tensile specimens.
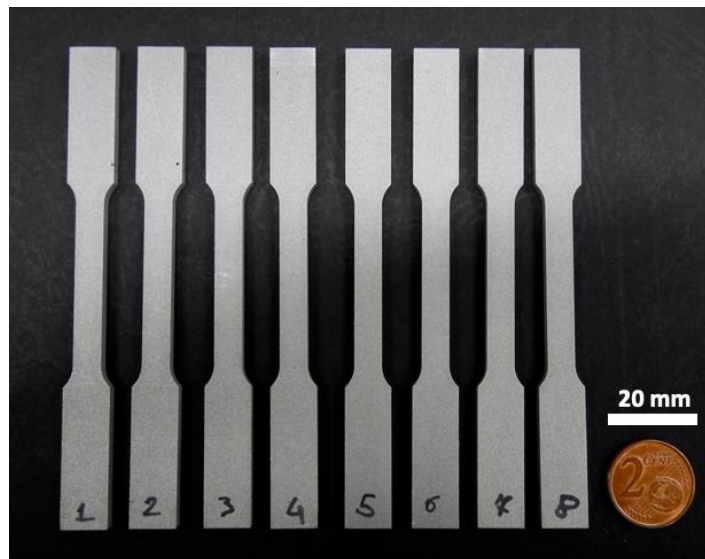

Figure 6 *Tensile dog bone-shaped specimens after EDM cutting*

2 Results
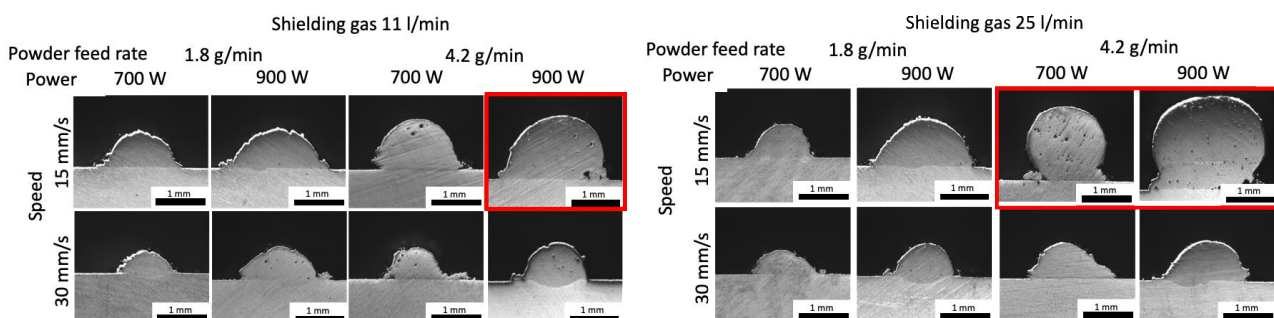
2.1 Single-track analysis and evidence

Figure 7 Cross-sections of single tracks

Fig. 7 shows a cross-section of singletrack deposits. In several processing conditions, pores are visible with a circular shape, which reveals a gas origin. The pores are more present at high power and low

speed when the energy content increases, promoting vaporisation and gas entrapment. In these conditions, the tracks' shape changes, resulting in an undesired condition (i.e. shown in red in Fig. 7). In these conditions, tracks are easily detached from the substrate, affecting the printing of 3D components. Their irregular shape can be classified as poor quality.

Fig. 8 shows the trend of the relative density as a function of varied parameters. The obtained values are always higher than 97%.
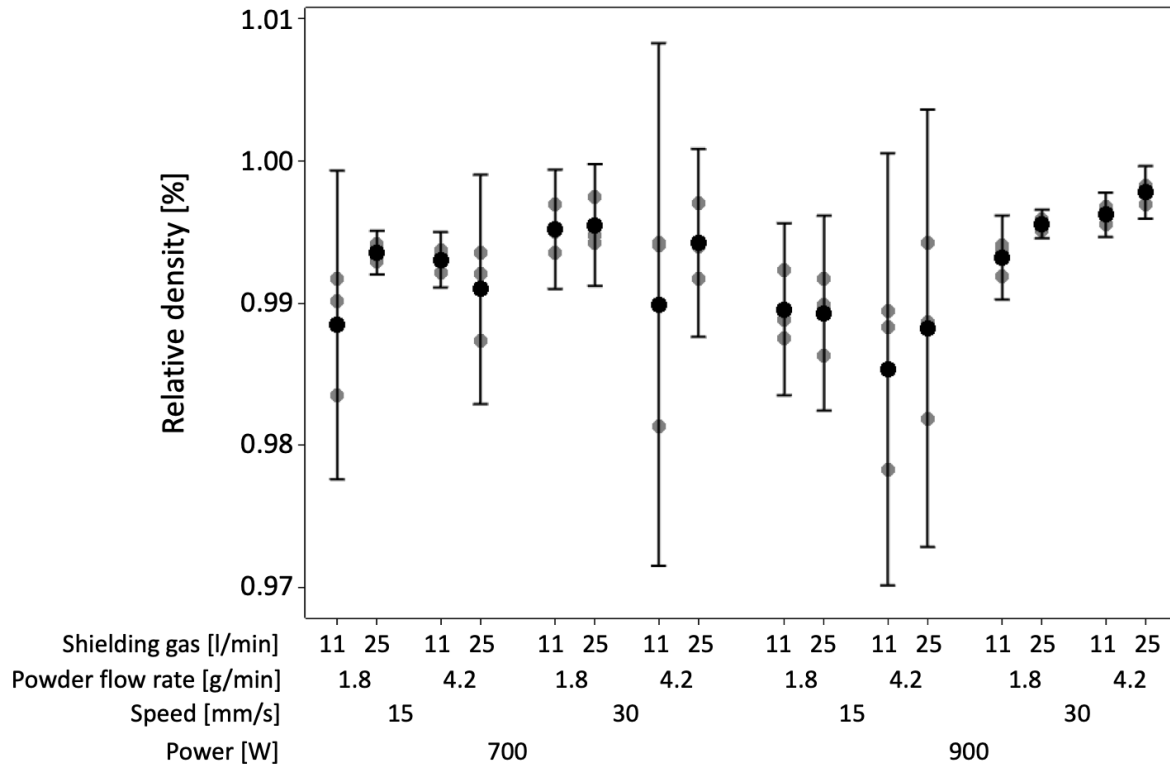

Shielding gas [l/min]	11	25	11	25	11	25	11	25	11	25	11	25	11	25	11	25
Powder flow rate [g/min]	1.8		4.2		1.8		4.2		1.8		4.2		1.8		4.2	
Speed [mm/s]	15				30				15				30			
Power [W]	700								900							

Figure 8 Individual plot of relative density of single-track deposit

Moreover, according to the graphs, the process parameters which result in the higher density are characterised by laser power of 900 W, scanning speed of 30 mm/s, powder flow rate of 4.2 g/min and shielding gas equal to 25 l/min.

Specifically, the shielding gas does not appear to have a significant influence on the density values. However, using a shielding gas flow rate of 25 l/min results in a slightly higher part density than when using a shielding gas flow rate of 11 l/min. Moreover, high shielding gas means better protection from oxidation. No detachment of this track from the substrate is observed.

This combination will be utilised in further experiments and these parameters are the starting point of multi-pass and multi-layer experiments.

2.2 Multi-pass and multi-layer analysis and evidence

In the multi-pass and multi-layer experiments, the influence of the flow rate of the carrier gas on the part properties is examined. Fig. 9 shows the printed cubes.
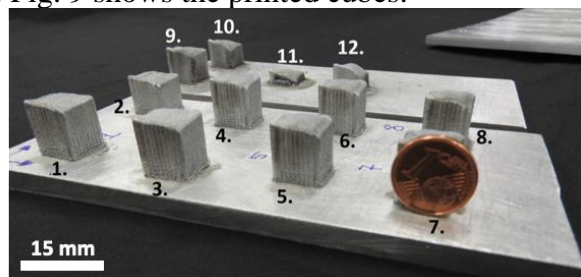

Figure 9 Multi-pass and multi-layer cubes with carrier gas as varied parameter

The carrier gas flow rate of 4.5 l/min does not permit the printing of cubes (i.e. cubes 10, 11 and 12 in Fig. 9). For this reason, these conditions are excluded from the further analyses.
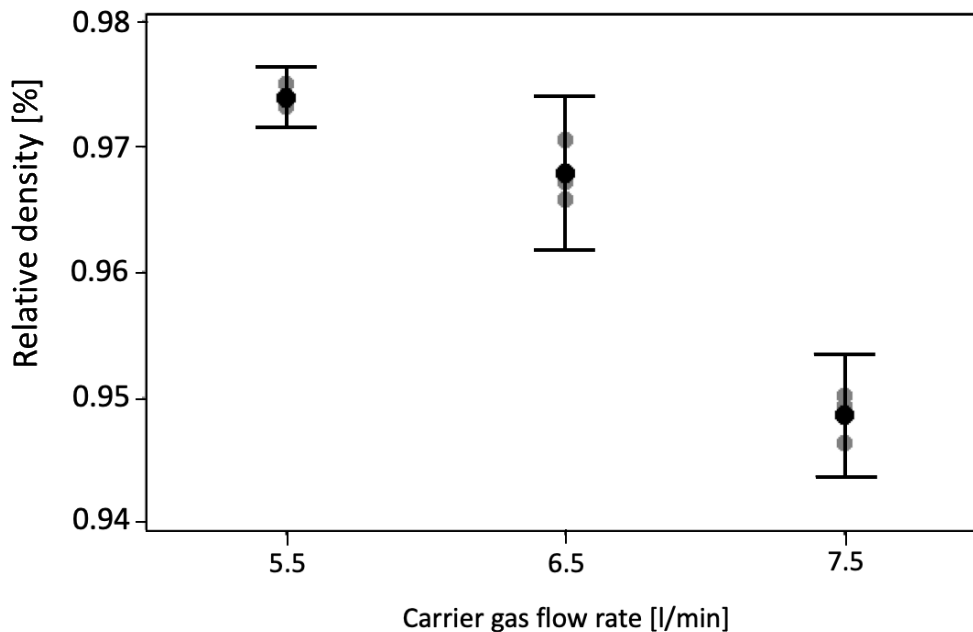

Figure 10 Interval plot of relative density for multi-pass and multi-layer cubes (95% CI for the mean)

The density results are shown in Fig. 10, from which it can be concluded that the carrier gas flow rate equal to 5.5 l/min achieves the highest density as well as the lowest standard deviation, which indicates that it is the best condition. Fig. 11 shows the three replicas with the best condition of carrier gas flow rate. The average relative density value is 97.4% ± 0.3%. It is interesting to observe that the reference values of relative density obtained in the literature are in the range of 85-90%, taking into account the LMD of Al-12Si alloys [20].
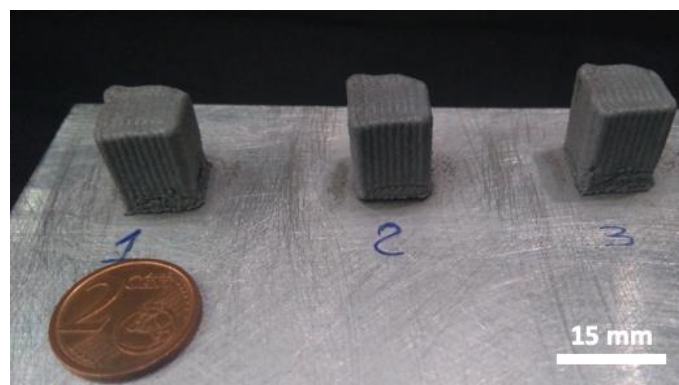

Figure 11 Three replicas with a condition of 5.5 l/min of carrier gas flow rate

Despite the higher density values of single tracks, the multi-pass and multi-layer parts reveal a lower part density due to the complexity and dynamics of melt pool behaviour in massive part production.
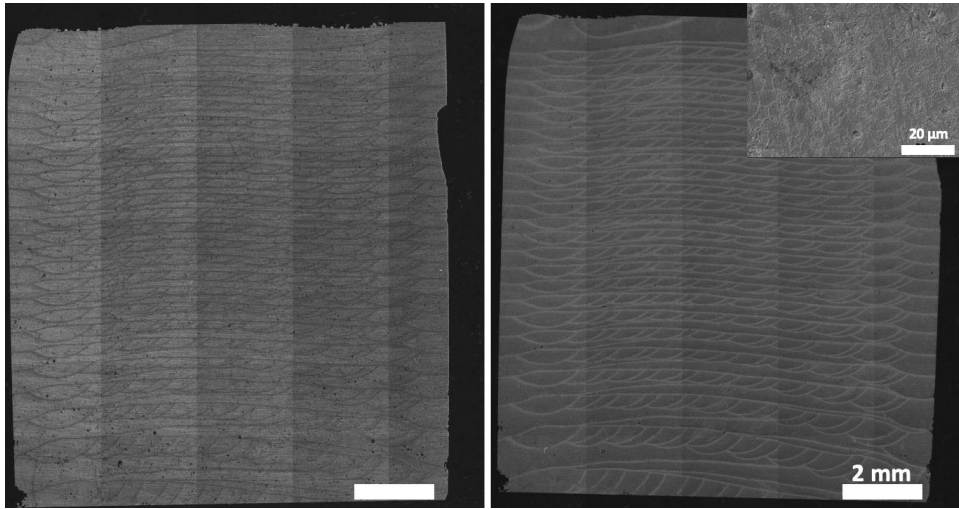
Figure 12 Cross-section of cubes printed with 5.5 l/min of carrier gas flow rate: on the left, the sample without etching, on the right, the sample etched and its microstructure

Fig. 12 shows the cross-section of cubes produced with 5.5 l/min of carrier gas flow rate. The sample without etching shows the porosities with a circular shape and stochastic distribution, confirming the gas origin. The chemical etching brings out passes and layers. The different behaviour of the first layers is evident. In the first layers, the layer height is higher than in the others. This condition is related to a different cooling rate, taking into account the effect of the substrate [38]. After these layers, the growth becomes stable. EDS analysis reveals that the oxygen percentage is qualitatively low. Analysis shows that the Mg content decreases from the nominal value of 0.65 to in the range of 0.3 on different sections of the deposit. In fact, Mg has a lower evaporation temperature compared to aluminum. Therefore, there is a risk of losing these elements in the process.. Table 6 shows the results of EDS analysis.

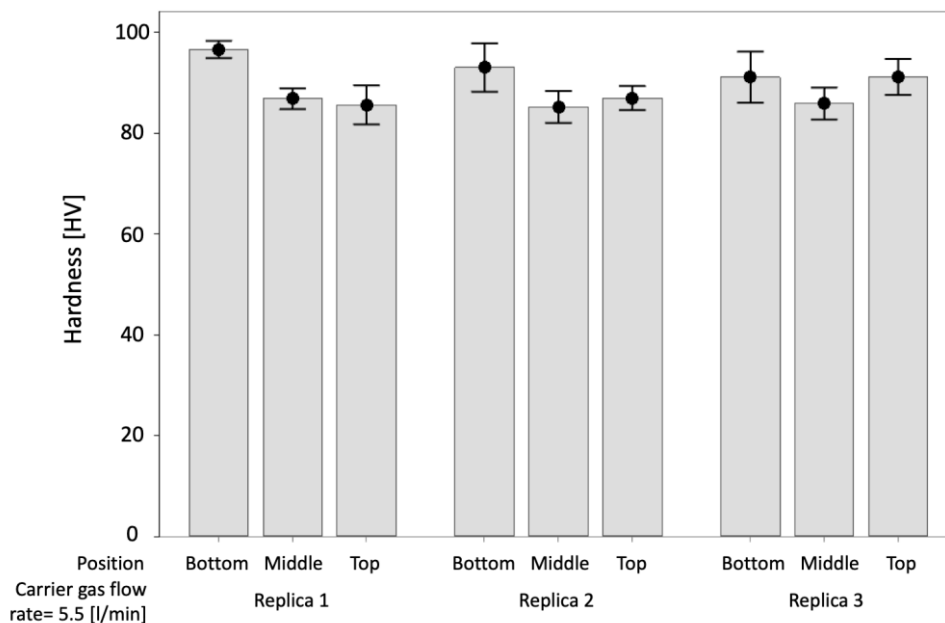| Element	wt%
Al	89.2 ±1.6
Si	10.5±1.6
Mg	0.3±0.1

Table 6 EDS analysis of validation run cubes

Figure 13 Microhardness measurements on the optimised cubic samples.

Fig. 13 shows the microhardness measurements. As already stated, the cooling rate in LMD is higher than in casting but lower than in SLM. Therefore, it is expected to obtain hardness values that are analogously higher than casting but lower than SLM. Casting hardness values are generally about 70 HV [39] and SLM hardness values are commonly determined higher than 100 HV [40]. Thus, the hardness values of selected cubes, found between 70 and 100 HV, clearly proves that the results are coherent. In terms of hardness, the cubes show comparable behaviour with the results from the literature. Dinda et al. [41] measured 107 HV and Mazumder et al. [19] measured hardness values from 77 to 90 HV for LMD-processed Al4047 alloy.

In some cases, the standard deviation seems high. The LMD process creates inhomogeneities inside the material and it is not possible to have low standard deviation and relatively stable hardness values at each layer. Also, 10 hardness values are measured per layer. While some measurements are taken from the track core, others are taken from the track boundary. This situation also results in different hardness values, even if they are taken from the same layer. Furthermore, it should be noted that the bottom part of the cubes has higher hardness values compared to the middle and top sections because the cooling rate is higher at the bottom due to the substrate.

2.3 Results on mechanical performance of printed specimens

Building direction might affect the mechanical properties of the fabricated part. To determine the difference between printed parts introduced by the building direction, one vertical and one horizontal parallelepiped are printed. Four dog bone samples are obtained from each parallelepiped to perform tensile tests. The vertical samples have a relative density equal to 98.29% ± 0.08, while horizontal samples have a relative density equal to 97.75% ± 0.49. Moreover, the values are aligned with the results of cubes with selected conditions. It is concluded that the process remains stable after some distance from the substrate. A cold substrate temperature makes the beginning of the process more unstable, therefore the porosity is present in the first layers compared to the other parts of the deposit. Generally, the vertically built samples have a higher density compared to the horizontal samples. In the case of the horizontal parallelepiped, there is more unstable volume at the lower level of the deposit compared to the vertical sample.

Fig. 14 shows the results from the tensile test on the horizontally and vertically printed specimens. The mechanical property results of specimens are shown in Table 7.
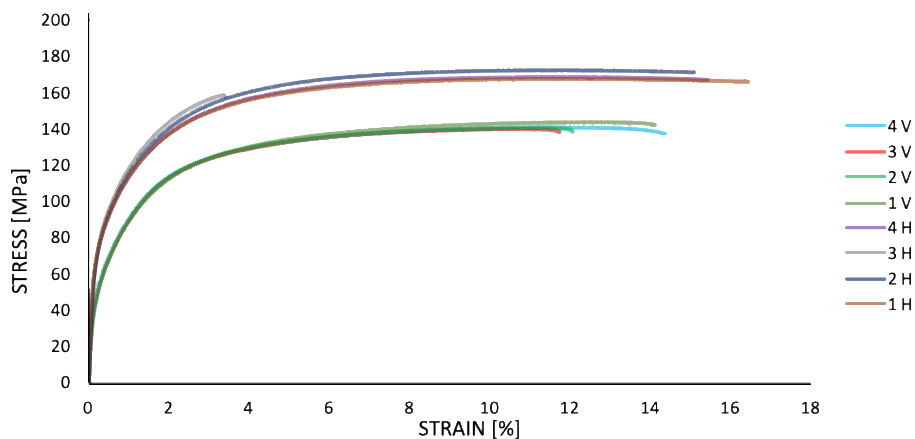

Figure 14 Stress-strain curve of horizontal (H) and vertical (V) test specimens

Specimen	Young's Modulus (MPa)	Yield Stress (MPa)	Ultimate Tensile Stress (MPa)	Fracture Stress (MPa)	Breaking Strain (%)
1 H	62.93	82.31	167.64	160.91	18.75
2 H	68.85	82.47	172.60	166.69	16.19

3 H	64.08	85.33	158.72	158.42	3.35
4 H	68.61	81.19	168.84	163.51	15.86
1 V	43.57	60.68	143.89	139.62	14.24
2 V	37.31	60.46	140.72	137.27	12.08
3 V	39.87	60.45	140.19	136.01	11.82
4 V	46.25	59.34	140.86	127.52	15.08

Table 7 Tensile test results of dog bone specimens

Horizontal samples perform better than vertical ones. Young's Modulus, yield stress, ultimate tensile stress (UTS) and breaking strain are higher for horizontal samples. However, except for Young's Modulus and fracture stress, the standard deviation of mechanical properties for vertical specimens is lower than for horizontal samples. Specimen 3H shows very fragile behaviour and lower density. The reason can be understood after fracture surface analysis, where unmelted powders were detected. For sample 3H, agglomerated unmelted powders are detected as shown in Fig. 15. This is most probably because when printing the horizontal parallelepiped, the working gas has finished and it is renewed. This stopping and restarting creates a problem with powder flowability, resulting in agglomerated unmelted powder present inside the deposit.
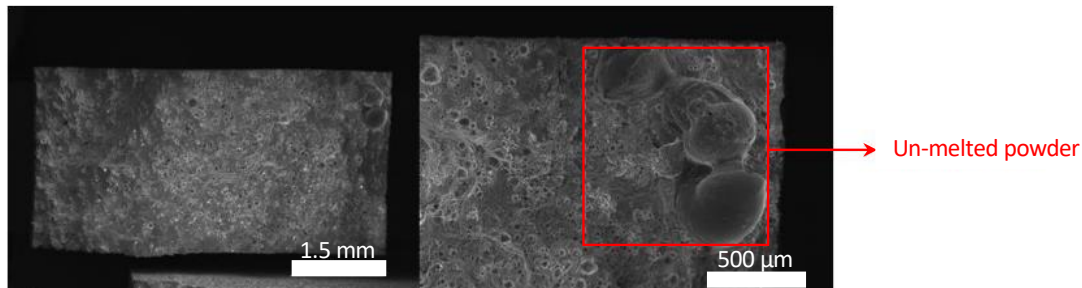

Figure 15 Fracture surface image of specimen 3H

After tensile tests, samples are cut vertically and horizontally in order to identify variations in the microstructure depending on the deposition direction. Both sections display a cellular and dendritic structure. In the XY plane (Fig. 16), cells are generally cellular, but in the YZ plane, (Fig. 17), the columnar structure is visible. This difference is caused by heat dissipation directions. In the YZ plane, heat goes through the substrate and cells stretch in the opposite direction to the heat flow. Thus, they become columnar. The circular structure is also caused by the heat dissipation direction in the XY plane. This view becomes the top view of the columnar structure. Therefore, only equiaxed structures are visible rather than columns.

When the microstructure of sections is checked with higher magnification, cells are visible. As the magnification is increased, it can be seen that the continuous network between Si particles starts to be destroyed and individual Si particles can be recognised, as visualised in Fig. 16 and Fig. 17.
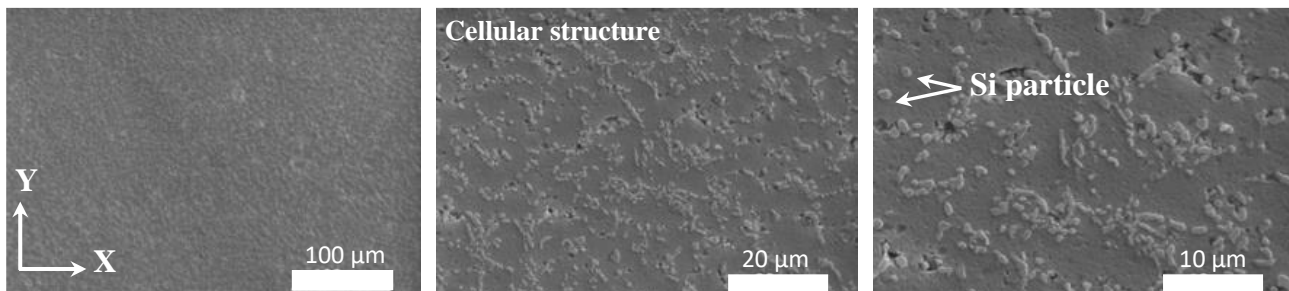

Figure 16 Different magnification microstructures from vertical tensile specimen (XY plane)
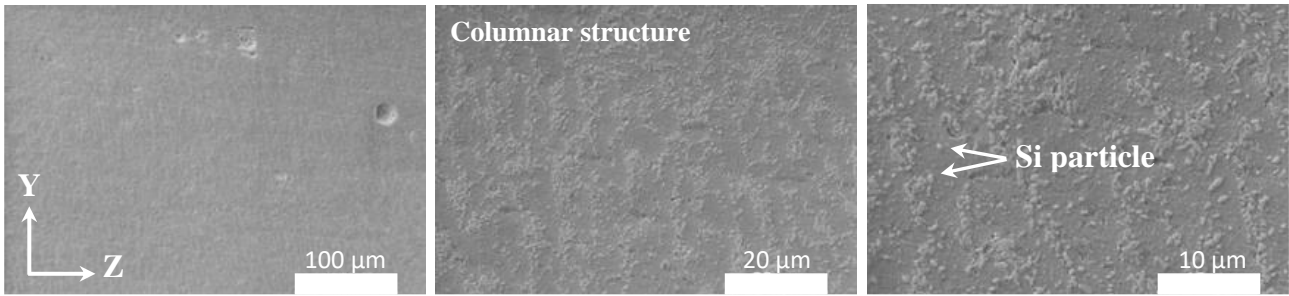
Figure 17 Different magnification microstructures from horizontal tensile specimen (YZ plane)

As a final step, fracture surfaces of specimens are analysed. The fracture surfaces of horizontally built specimens are wavier than the vertically built samples, which verifies the higher elongation and ductility of samples obtained in the tensile test. However, it is possible to see cup and cone shapes for both vertical and horizontal constructions thanks to the ductile nature of the aluminum alloy. Also, the fracture surface of samples has an extremely fine roughness, which is made by microvoids and dimples that are formed during the yielding of material (Fig. 18).
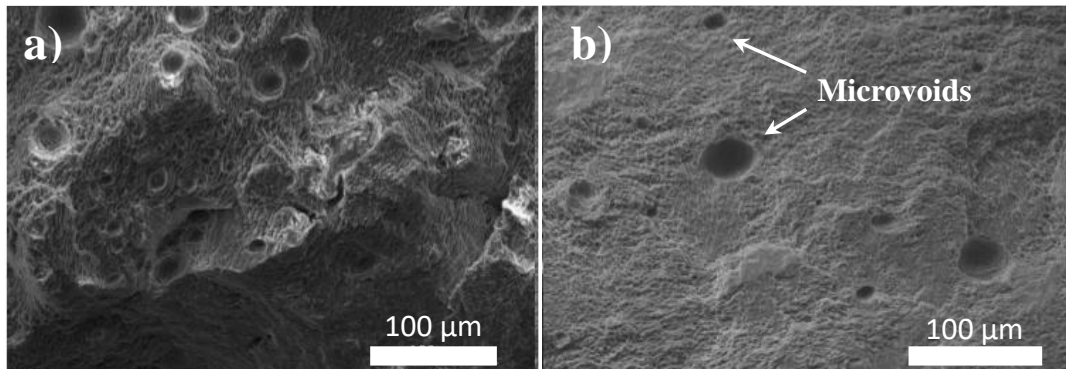

Figure 18 Representative examples of fracture surfaces, (a) Horizontally built sample (b) Vertically built sample

3 Discussion

Cubes are basic shapes useful for gathering information for further production steps. The microstructure of cubes is analysed by SEM (Fig. 19) and it reveals Si particles that are connected to each other with an equiaxed microstructure.
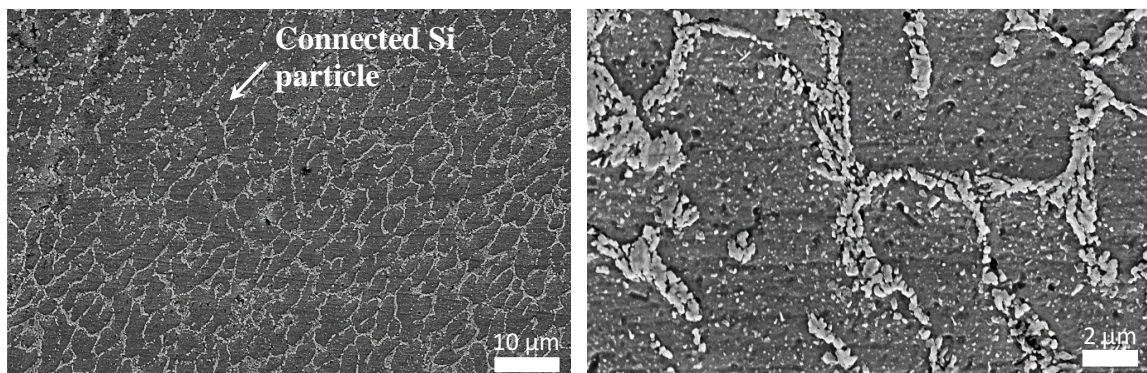
Figure 19 SEM images of one of the selected cubes

The cellular structure is dominant in the cubes thanks to the high cooling rate, which does not allow the growth of Si particles, and the cellular structure provides higher levels of hardness thanks to the interconnection between Si particles compared to a coarser structure [20], [41], [42]. On the other hand, these connections do not allow dislocations to go through them easily, so high strength can be obtained.

After the cube microstructure is analysed, tensile test specimens are investigated.

Moreover, the heat treatment reveals a different microstructure. The continuous network between Si particles is destroyed and individual Si particles can be recognised. The difference can be seen more clearly, especially if the microstructure is compared with validation run cubes. The resulting microstructure is made by the homogenous distribution of globular Si particles on grain boundaries together with a saturated Al matrix. The transition of needle-shaped Si crystals to a coarser cubic shape is clearly visible in Fig. 20, where the comparison between non-treated and heat-treated samples is shown.
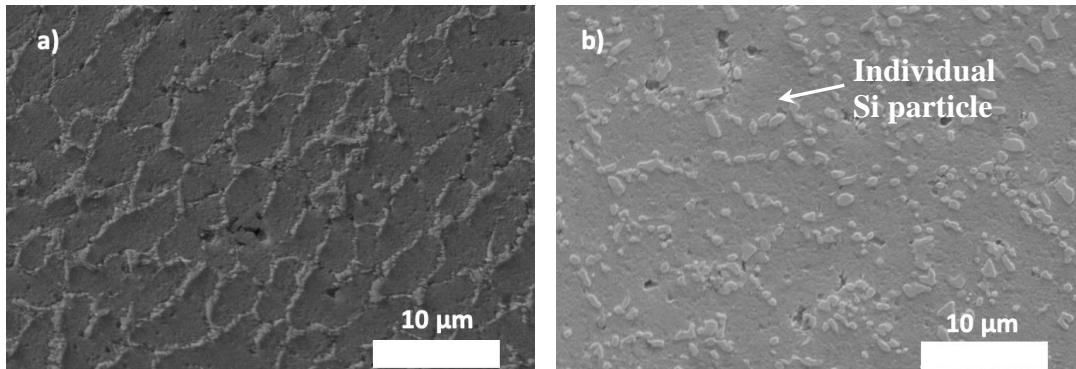

Figure 20 Microstructure a) Non-heat-treated sample b) Heat-treated sample.

Despite higher values of porosity in horizontal dog bone samples, building in a horizontal direction is more advantageous than building in a vertical direction in terms of strength and elongation, as shown in Fig. 14 and Table 7. This is mainly due to the fact that for horizontally built parts, the loading direction is parallel to the layers' planes, and some planes behave as reinforcing planes. On the other hand, the loading direction tends to separate layers because it is perpendicular to the deposit layer plane for vertically built samples. The second possibility for this difference can be a major axis of defects. In vertically built samples, the major axis of defects is perpendicular to the tensile load direction, which results in higher stress concentration and easier crack propagation. On the other hand, for horizontally built samples, the loading axis is parallel to the major axis of defects, which gives rise to lower stress concentration and higher crack resistance, and consequently higher elongation and tensile strength [43]. Furthermore, vertically built samples are ruptured from the same zones, i.e. the middle of the samples. This can be explained from the fact that these regions can have a smaller area than another part of the specimen or that this region is subjected to higher residual stress because of instabilities in the process and a higher thermal gradient. On the other hand, horizontally built samples can fracture in different zones. This can be seen as an indicator of homogenous microstructure and randomly distributed defects in the material. Thirdly, the orientation and number of damaged Si particles determine the ductility and UTS properties of the deposits. In the XY plane (Fig. 5), Si particles are tiny and they create small cells. However, in the YZ plane (Fig. 5), Si particles are coarser and elongated in the direction of the heat flow. This type of Si particle is flimsier than tiny ones and it is easier to damage them. As a result, elongation is lower for vertically built specimens [17]. This is also one of the reasons why horizontally built samples have higher UTS values than vertically built samples.

Lastly, even though the density values of vertically built specimens are relatively higher than in horizontally built samples, they exhibit a more fragile behaviour. Generally, porosities found in vertically built samples are bigger, and bigger porosity dimples are observed in the fracture surfaces of vertically built samples. These porosities can be the cause of lower elongation and ductility [44]. Fig. 21 shows the described trend with pores characterised by a bigger dimension in the vertical dog bone-shaped samples.
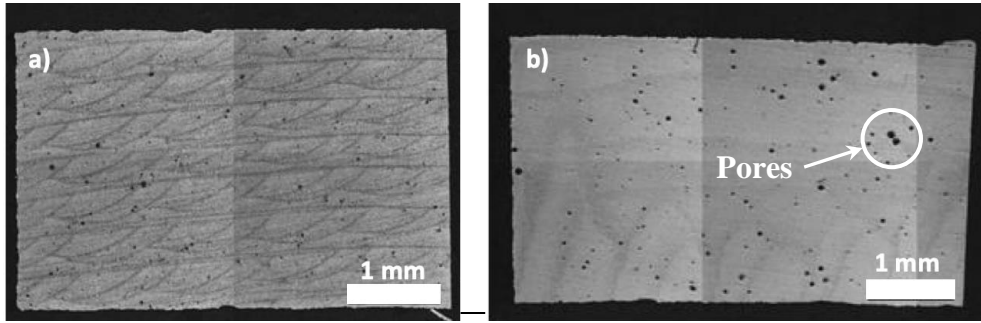
Figure 21 Cross-sections of a portion of dog bone samples: a) Horizontal sample, b) Vertical sample

Nevertheless, pores are present in printed samples and mostly spherical-shaped pores are detected. Spherical-shaped pores are an indication of trapped gas inside the material, and generally the pore size changes from 5 µm to 100 µm (Fig. 22).
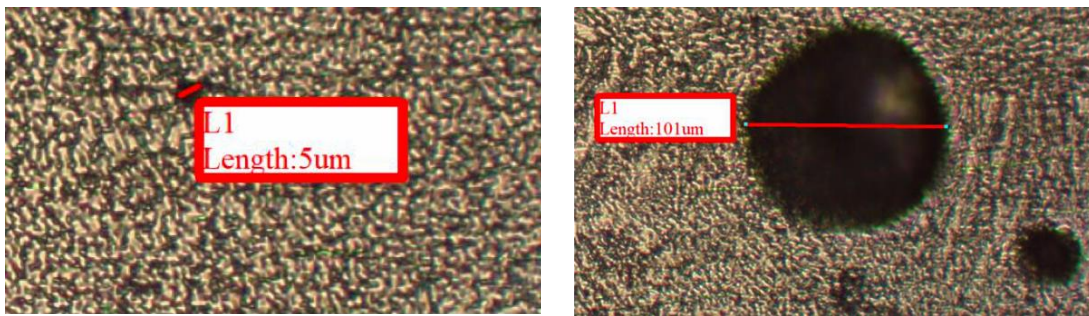

Figure 22 Detected spherical pores from cross-sections of samples

Some possible mechanisms might create such porosities. The evaporation of elements with a low melting temperature is a possible reason; this is also verified in the previous section by checking their quantity in SEM, resulting in a reduced amount of Mg. High temperature differences in melt pools may be another reason, and it can create unstable melt pools and, as a result, pores. However, this is a problem in regions that are close to the substrate. When cross-sections are analysed, even if more pores are presented in the bottom parts, there are still many pores in the middle and top parts too. Therefore, this cannot be the main cause of pores. Hydrogen pores can be in small sizes with a maximum of 10 µm. However, generally, pores that are larger than 10 µm are detected. To conclude, the main reason cannot be hydrogen agglomeration inside the material. Marangoni flow seems to be the main cause of such porosities, and with this flow, the working gas argon is trapped during the process. In tensile tests, these mechanisms must be considered.

When experimental results are compared to other studies in the literature, as reported in Table 8, it is clear to see that the mechanical properties of specimens are lower than in other studies on different alloys, with reference to the LMD process. For example, in the study of Dinda et al. [41], they obtained samples with UTS 225.7 MPa for Al12Si alloy with 9% elongation, and in the study of Lv et al. [45], 292 MPa is obtained from AlSi10Mg alloy with 6.7% elongation. Also, the nominal strength value of A357 alloy for casting is reported as 315 with 3% elongation [46]. Very high elongation and lower strength values compared to nominal situations may also be attributed to excessive heat treatment.

Year	Material	Process	Reference	Hardness (HV)	Relative Density (%)	Archimedes Density (g/cm^3)	UTS (MPa)	Yield Strength (MPa)	Break Elongation (%)
2020	A357	Casting	[14]	87	-	-	212	131	6.7
2003	A357	Casting	[47]	88	-	-	250	130	18
2014	A357	Casting	[48]	-	-	-	176.47	162.94	1.47
2009	A357	Casting	[49]	125±5	-	-	308±15	275±11	2±0.5
2014	A357	Under Pressure Casting	[18]	-	99.57	-	300	205	3.3

2018	A357	Rheo Diecasting	[50]	-	99.6	-	274	-	4.9
2011	A357	Thixoforging	[51]	-	-	2.55-2.68	391	315	8.8
2018	A357	LPBF	[16]	-	99.3	-	284±19 (H) 305±15 (V)	184±17 (H) 192±17 (V)	10,1±0,5 (H) 5,1±0,4 (V)
2020	AlMg4.5Mn0.7	WAAM	[52]	75-79	-	-	276.2±5.1 to 285.6±1.2	124.0±1.0 to 129.0±0.3	18.3±2.5 to 28.4±0.2
2016	A357	SLM	[17]	-	99.57±0.11	2.674	426.4±2.6 (H) 395.6±4.7 (V)	279.6±1 (H) 232.2±0.7 (V)	10.1±0.5 (H) 5.1±0.4 (V)
2018	A357	SLM	[15]	-	99.4±0.1	-	375	225	5.5
2019	A357	SLM	[47]	-	99.7	-	398±13 (H) 400±4 (V)	257±3 (H) 216±2 (V)	7.6±1.8 (H) 6.9±0.4 (V)
2017	A357	SLM	[53]	-	-	-	426.4±2.6	279.6±1	10.1±0.5
2016	A357	SLM	[40]	120	99.94±0.06	-	388±5	244±5	5.3±0.4
2017	Al12Si	LMD	[9]	70-90	-	-	225.7	122.43	-
2011	Al11.28Si	LMD	[41]	107	-	-	-	-	-
2012	Al4047	LMD	[19]	77-93					
2016	AlSi10Mg	LMD	[23]	53-65	99.6	2.67	-	-	-
2019	AlSi10Mg	LMD	[45]	101-121	99.4	-	292	-	6.5

Table 8 Mechanical properties of some aluminum alloys with different manufacturing processes

To conclude, in Table 9, a summary of obtained main results is reported. Specimens printed with the best parameters are characterized by relative densities higher than 97.5%. This condition is a starting point for further investigation focusing the attention on scanning strategies and different heat treatments. Moreover, hardness values are aligned with the literature and conventional manufacturing methods.

Relative Densities [%]	Hardness [HV]	Young's Modulus [MPa]	UTS [MPa]	Yield Strength [MPa]	Break Elongation [%]
H >97.5 V >98.3	80-100	H - 66.1±3.1 V- 41.8±4.0	H - 167.0±5.9 V - 141.4 ±1.7	H - 82.8±1.8 V - 60.2±0.6	H - 13.5±6.9 V -13.3±1.6

Table 9 Main results and characteristics of printed specimens

Finally low mechanical performance can be attributed to 3 problems: i) thermal treatment ii) loss of Mg content iii) porosities. All of these aspect can be investigated considering experimental campaign on different thermal treatments, and working with different spot diameters and energy distribution to modify the energy contents promoting a better beam-material interaction.

4 Conclusion

The laser metal deposition process was implemented successfully to produce A357 alloy samples. A preliminary experimental campaign on single-track deposition enabled the definition of best-process parameters in terms of power, speed, powder feed rate, carrier gas flow rate and shielding gas flow rate. Multi-pass and multi-layer experiments were conducted to investigate different carrier gas flow rates. The best condition was identified and the cubes obtained revealed a density higher than 97% and a microhardness in the range of 80-100 HV. The hardness values are aligned with the reference for the present material. The selected condition also showed a clear cellular and columnar structure with very fine interconnected Si particles, nevertheless a loss of Mg elements was observed, as well as porosity formation. The LMD of A357 presents higher porosities if compared with values of samples printed with the same material and SLM technology. Nevertheless, the obtained result is the starting point for further analysis considering different scanning strategies, thermal treatments, and energy contents of working spot diameter. A further increase in specimen density can promote the use of LMD for the production of large components in several fields.

The produced tensile specimens were tested in two printing directions. Horizontally built samples produced better mechanical performances, even if their density values were slightly lower than those in vertically built samples. Despite UTS, yield strength and elongation presenting lower values in

comparison with casted or SLM samples, the results obtained are promising for further investigation given the lack of evidence on A357 and LMD. The first comprehensive study on A357 underlined the first best set of printing parameters to obtain high-density values as much as good mechanical performances. It focuses attention on the usability of LMD technology, as an alternative to the other additive manufacturing technologies with aluminum, considering LMD flexibility in the fabrication and repairing of existing and complex components.

Acknowledgements

References

[1]   D. Cao, S. Malakooti, V. N. Kulkarni, Y. Ren, Y. Liu, X. Nie, D. Qian, D. T. Griffith, and H. Lu, 'The effect of resin uptake on the flexural properties of compression molded sandwich composites', *Wind Energy*, vol. 25, pp. 71–93, 2022.

[2]   D. Cao, S. Malakooti, V. N. Kulkarni, Y. Ren, and H. Lu, 'Nanoindentation measurement of core – skin interphase viscoelastic properties in a sandwich glass composite', *Mech Time-Depend Mater*, vol. 25, pp. 353–363, 2021.

[3]   J. Den Boer, W. Lambrechts, and H. Krikke, 'Additive manufacturing in military and humanitarian missions : Advantages and challenges in the spare parts supply chain', *J. Clean. Prod.*, vol. 257, p. 120301, 2020.

[4]   Y. Kok, X. P. Tan, P. Wang, M. L. S. Nai, N. H. Loh, E. Liu, and S. B. Tor, 'Anisotropy and heterogeneity of microstructure and mechanical properties in metal additive manufacturing : A critical review', *Mater. Des.*, vol. 139, pp. 565–586, 2018.

[5]   N. Shamsaei, A. Yadollahi, L. Bian, and S. M. Thompson, 'An overview of Direct Laser Deposition for additive manufacturing; Part II: Mechanical behavior, process parameter optimization and control', *Addit. Manuf.*, vol. 8, pp. 12–35, 2015.

[6]   L. Zhu, P. Xue, Q. Lan, G. Meng, Y. Ren, and Z. Yang, 'Recent research and development status of laser cladding : A review', *Opt. Laser Technol.*, vol. 138, no. 106915, pp. 1–26, 2021.

[7]   L. Zhu, S. Wang, H. Pan, C. Yuan, and X. Chen, 'Research on remanufacturing strategy for 45 steel gear using H13 steel powder based on laser cladding technology', *J. Manuf. Process.*, vol. 49, pp. 344–354, 2020.

[8]   L. Zhu, S. Wang, H. Lu, D. Qi, D. Wang, Z. Yang, J. Ning, Y. Dun, P. Xue, P. Xu, B. Xin, L. Zhu, S. Wang, H. Lu, D. Qi, D. Wang, and Z. Yang, 'Investigation on synergism between additive and subtractive manufacturing for curved thin-walled structure', *Virtual Phys. Prototyp. ISSN*, vol. 17, no. 2, pp. 220–238, 2022.

[9]   Y. Xuan and L. Nastac, 'TMS 2017 146th Annual Meeting & Exhibition Supplemental Proceedings', in *Microstructure Characteristics of A356 Nanocomposites Manufactured via Ultrasonic Cavitation Processing Under Controlled Solidification Conditions*, 2017, pp. 297–303.

[10]   B. Haldar and P. Saha, 'Identifying defects and problems in laser cladding and suggestions of

some remedies for the same', *Mater. Today Proc.*, vol. 5, pp. 13090–13101, 2018.

[11]   A. Wang, H. Wang, Y. Wu, and H. Wang, '3D printing of aluminum alloys using laser powder deposition : a review', *Int. J. Adv. Manuf. Technol.*, vol. 116, pp. 1–37, 2021.

[12]   ASTM F3187-16, 'Standard Guide for Directed Energy Deposition of Metals'. pp. 1–22, 2018.

[13]   S. Wang, J. Ning, L. Zhu, Z. Yang, W. Yan, Y. Dun, P. Xue, P. Xu, S. Bose, and A. Bandyopadhyay, 'Role of porosity defects in metal 3D printing : Formation mechanisms , impacts on properties and mitigation strategies', *Mater. Today*, vol. 59, pp. 133–160, 2022.

[14]   G. Asghar, L. Peng, P. Fu, L. Yuan, and Y. Liu, 'Role of Mg2Si precipitates size in determining the ductility of A357 cast alloy', *Mater. Des.*, vol. 186, p. 108280, 2020.

[15]   K. V Yang, P. Rometsch, C. H. J. Davies, A. Huang, and X. Wu, 'Effect of heat treatment on the microstructure and anisotropy in mechanical properties of A357 alloy produced by selective laser melting', *Mater. Des.*, vol. 154, pp. 275–290, 2018.

[16]   L. Denti, 'Tensile Performance', *Metals (Basel).*, vol. 8, no. 670, pp. 1–15, 2018.

[17]   H. Rao, S. Giet, K. Yang, X. Wu, and C. H. J. Davies, 'The influence of processing parameters on aluminium alloy A357 manufactured by Selective Laser Melting', *Mater. Des.*, vol. 109, pp. 334–346, 2016.

[18]   B. Xiong, X. Lin, Z. Wang, Q. Yan, and H. Yu, 'Microstructures and mechanical properties of vacuum counter-pressure casting A357 alloy under grade-pressurizing solidification: Effect of melt temperature', *Mater. Sci. Eng. A*, vol. 611, pp. 9–14, 2014.

[19]   G. P. Dinda, A. K. Dasgupta, S. Bhattacharya, H. Natu, and B. Dutta, 'Microstructural Characterization of Laser-Deposited Al 4047 Alloy', *Metall. Mater. Trans. A*, vol. 44, no. May, 2013.

[20]   S. Lathabai, 'Additive Manufacturing of Aluminium-Based Alloys and Composites', in *Fundamentals of Aluminium Metallurgy*, Elsevier Ltd., 2018, pp. 47–92.

[21]   S. P. Isanaka, S. Karnati, and F. Liou, 'Blown powder deposition of 4047 aluminum on 2024 aluminum substrates', *Manuf. Lett.*, vol. 7, no. 2016, pp. 11–14, 2024.

[22]   A. Singh, A. Ramakrishnan, and G. P. Dinda, 'TMS 2017 146th Annual Meeting & Exhibition Supplemental Proceedings', in *Direct Laser Metal Deposition of Eutectic Al-Si Alloy for Automotive Applications*, 2017, pp. 71–80.

[23]   M. Javidiani, Arreguin-Zavala, J. Danovitch, Y. Tian, and M. Brochu, 'Additive Manufacturing of AlSi10Mg Alloy Using Direct Energy Deposition : Microstructure and Hardness Characterization', *J. Therm. Spray Technol.*, vol. 26, no. 4, pp. 587–597, 2017.

[24]   B. Chen, Y. Yao, X. Song, C. Tan, L. Cao, and J. Feng, 'Microstructure and mechanical properties of additive manufacturing AlSi10Mg alloy using direct metal deposition', *Ferroelectrics*, vol. 523, pp. 153–166, 2018.

[25]   K. Zyguła, B. Nosek, H. Pasiowiec, and N. Szysiak, 'Mechanical properties and microstructure of AlSi10Mg alloy obtained by casting and SLM technique', *World Sci. News*, vol. 104, no. February 2019, pp. 462–472, 2018.

[26]   A. F. Lv, L. Shen, H. Liang, and D. Xie, 'Mechanical Properties of AlSi10Mg Alloy

Fabricated by Laser Melting Deposition and Improvements via Heat Treatment', *Opt. -*, vol. 179, pp. 8–18, 2019.

[27]   G. Cao and S. Kou, 'Liquation Cracking in Full Penetration Al-Si Welds', *Weld. J.*, vol. 84, no. 4, pp. 63–71, 2005.

[28]   S. Liu, J. Zhu, H. Zhu, J. Yin, C. Chen, and X. Zeng, 'Effect of the track length and track number on the evolution of the molten pool characteristics of SLMed Al alloy : Numerical and experimental study', *Opt. Laser Technol.*, vol. 123, no. October, p. 105924, 2020.

[29]   X. Liu, C. Zhao, X. Zhou, Z. Shen, and W. Liu, 'Microstructure of selective laser melted AlSi10Mg alloy', *Mater. Des.*, vol. 168, p. 107677, 2019.

[30]   A. Ramakrishnan and G. P. Dinda, 'Microstructural control of an Al e W aluminum matrix composite during direct laser metal deposition', *J. Alloys Compd.*, vol. 813, p. 152208, 2020.

[31]   J. Xiong, Y. Lei, and R. Li, 'Finite element analysis and experimental validation of thermal behavior for thin-walled parts in GMAW-based additive manufacturing with various substrate preheating temperatures', *Appl. Therm. Eng.*, vol. 126, pp. 43–52, 2017.

[32]   D. Yang, G. Wang, and G. Zhang, 'Thermal analysis for single-pass multi-layer GMAW based additive manufacturing using infrared thermography', *J. Mater. Process. Tech.*, vol. 244, pp. 215–224, 2017.

[33]   J. Xie and A. Kar, 'Laser Welding of Thin Sheet Steel with Surface Oxidation', *Weld. Res. Suppl. /*, pp. 343–348, 1999.

[34]   A. B. Spierings, M. Schneider, I. Ag, U. I. Ag, and S. Gallen, 'Comparison of density measurement techniques for additive manufactured metallic parts', *Rapid Prototyp. J.*, vol. 5, no. February 2010, pp. 380–386, 2011.

[35]   Y. Gao, J. Zhao, Y. Zhao, Z. Wang, H. Song, and M. Gao, 'Effect of processing parameters on solidification defects behavior of laser deposited AlSi10Mg alloy', *Vacuum*, vol. 167, no. May, pp. 471–478, 2019.

[36]   *ASM Handbook - Volume 2 Properties and Selection: Nonferrous Alloys and Special-Purpose Materials*. 2001.

[37]   B. W. Xiong, H. Yu, Q. S. Yan, J. Q. Zhao, S. N. Chen, and Z. Yang, 'Effects of sample thickness on microstructures and mechanical properties of A357 alloy', *Int. J. Cast Met. Res.*, vol. 25, no. 6, pp. 2–7, 2012.

[38]   S. Donadello, V. Furlan, A. Gökhan, and B. Previtali, 'Interplay between powder catchment efficiency and layer height in self-stabilized laser metal deposition', *Opt. Lasers Eng.*, vol. 149, no. August 2021, p. 106817, 2022.

[39]   Y. Tzeng, V. Chengn, J. Nieh, H. Bor, and S. Lee, 'Microstructure and Thermal Stability of A357 Alloy With and Without the Addition of Zr', *J. Mater. Eng. Perform.*, 2017.

[40]   F. Trevisan, F. Calignano, M. Lorusso, J. Pakkanen, E. Ambrosio, M. Lombardi, M. Pavese, D. Manfredi, and P. Fino, 'Effects of Heat Treatments on A357 Alloy Produced by Selective Laser Melting', *World PM2016 – AM - Prop. Light. Mater. I 110*, pp. 1–7, 2016.

[41]   G. P. Dinda, A. K. Dasgupta, and J. Mazumder, 'Evolution of microstructure in laser deposited Al – 11 . 28 % Si alloy', *Surf. Coat. Technol.*, vol. 206, no. 8–9, pp. 2152–2160,

2012.

[42] R. Trivedi, F. Jin, and I. E. Anderson, 'Dynamical evolution of microstructure in finely atomized droplets of Al-Si alloys', *ACS Appl. Mater. Interfaces*, vol. 51, pp. 289–300, 2003.

[43] H. Asgari, C. Baxter, and M. Mohammadi, 'On microstructure and mechanical properties of additively manufactured AlSi10Mg_200C using recycled powder', *Mater. Sci. Eng. A*, vol. 707, pp. 148–158, 2017.

[44] P. Guo, B. Zou, C. Huang, and H. Gao, 'Study on microstructure , mechanical properties and machinability of efficiently additive manufactured AISI 316L stainless steel by high-power direct laser deposition', *J. Mater. Process. Tech.*, vol. 240, pp. 12–22, 2017.

[45] F. Lv, L. Shen, H. Liang, D. Xie, C. Wang, and Z. Tian, 'Mechanical properties of AlSi10Mg alloy fabricated by laser melting deposition and improvements via heat treatment', *Opt. - Int. J. Light Electron Opt.*, vol. 179, no. October 2018, pp. 8–18, 2019.

[46] J. G. Kaufman and E. L. Rooy, *Aluminum Alloy Castings Properties , Processes , and Applications*. 2004.

[47] N. D. Alexopoulos and S. G. Pantelakis, 'Quality evaluation of A357 cast aluminum alloy specimens subjected to different artificial aging treatment', *Mater. Des.*, vol. 25, pp. 419–430, 2004.

[48] Z. Chen, X. Hao, Y. Wang, and K. Zhao, 'In-situ Observation of Tensile Fracture in A357 Casting Alloys', *J. Mater. Sci. Technol.*, vol. 30, no. 2, pp. 139–145, 2014.

[49] L. Ceschini, A. Morri, A. Morri, A. Gamberini, and S. Messieri, 'Correlation between ultimate tensile strength and solidification microstructure for the sand cast A357 aluminium alloy', *Mater. Des.*, vol. 30, no. 10, pp. 4525–4531, 2009.

[50] A. Guo, J. Zhao, C. Xu, H. Li, J. Han, and X. Zhang, 'Effects of Pouring Temperature and Electromagnetic Stirring on Porosity and Mechanical Properties of A357 Aluminum Alloy Rheo-Diecasting', no. Ref 18, 2018.

[51] Z. Du, G. Chen, and S. Xie, 'Inhomogeneity of density and mechanical properties of A357 aluminum alloy backward extruded in semi-solid state', *Trans. Nonferrous Met. Soc. China*, vol. 21, no. 10, pp. 2285–2293, 2011.

[52] T. Klein and M. Schnall, 'Control of macro- / microstructure and mechanical properties of a wire-arc additive manufactured aluminum alloy', *Int. J. Adv. Manuf. Technol.*, vol. 108, pp. 235–244, 2020.

[53] J. H. Rao, Y. Zhang, X. Fang, Y. Chen, X. Wu, and C. H. J. Davies, 'The origins for tensile properties of selective laser melted aluminium alloy A357', *Addit. Manuf.*, vol. 17, pp. 113–122, 2017.